J Nanostruct 16(3): 3884-3903, Summer 2026

RESEARCH PAPER

Silver and Zinc Oxide Nanoparticles: Mechanisms of Antimicrobial Activity and Potential Applications in Wound Dressing

Uktam Fozilov [1] *, Sitora Rakhimova [2], Saydillo Jamoldinov [3], Rano Muslimova [4], Madiba Erkinova [5], Charos Raimova [6], Farrukhbek Khamidov [7], Gulshoda Fatilloyeva [8], Gulnora Akramova [9], Rustam To'laganov [10], Sulaymon Buriyev [11], Gulchexra Ishkabulova [12], Nilufar Kurbonova [13]

[1] *Department of Orthopedist Dentistry and Orthodontics, Bukhara State Medical Institute named after Abu Ali ibn Sino, Bukhara, Uzbekistan*

[2] *Department of Internal Medicine 2 and Endocrinology, Tashkent Medical University, Tashkent, Uzbekistan*

[3] *Department of Computer Engineering, State University, Andijan, Uzbekistan*

[4] *Tashkent State Technical University named after I. Karimov, Tashkent, Uzbekistan*

[5] *Tashkent Institute of Irrigation and Agricultural Mechanization Engineers, National Research University, Tashkent, Uzbekistan*

[6] *Department of Food Technology (Biotechnology), Gulistan State University, Gulistan, Syrdarya, Uzbekistan*

[7] *Department of Dermatovenereology, Andijan State Medical Institute, Andijan, Uzbekistan*

[8] *Department of Phthisiology and Pulmonology of the Bukhara State Medical Institute named after Abu Ali ibn Sino Bukhara, Uzbekistan*

[9] *Tashkent University of Information Technologies named after Muhammad al-Khwarizmi, Tashkent, Uzbekistan*

[10] *Department of Sports Management, Termez State University, Surkhandarya, Uzbekistan*

[11] *Department of Biotechnology and Food Safety, Bukhara State University, Bukhara, Uzbekistan*

[12] *Department of Pediatrics of the Faculty of Medicine Samarkand State Medical University, Samarkand, Uzbekistan*

[13] *Department of English Translation Theory, Faculty of Translation, Uzbekistan State World Languages University, Tashkent, Uzbekistan*

ARTICLE INFO

Article History:
Received 27 March 2026
Accepted 25 June 2026
Published 01 July 2026

Keywords:
Antimicrobial activity
Biofilm inhibition
Silver oxide nanoparticles
Synergistic effect
Wound dressing
Zinc oxide nanoparticles

ABSTRACT

The escalating prevalence of antibiotic-resistant wound infections necessitates the development of alternative antimicrobial strategies. This study reports the synthesis, characterization, and comparative evaluation of zinc oxide (ZnO) and silver oxide (Ag_2O) nanoparticles as potential antimicrobial agents for wound dressing applications. Nanoparticles were prepared via simple precipitation routes, yielding ZnO NPs with spherical morphology (mean diameter 34.2 nm) and Ag_2O NPs with cubic to polyhedral shapes (mean diameter 42.5 nm). Structural characterization by FE-SEM, TEM, FT-IR, and XRD confirmed the high purity and crystallinity of both nanomaterials, with ZnO exhibiting single-crystalline wurtzite structure while Ag_2O formed polycrystalline aggregates with an average crystallite size of 23.6 nm. Antimicrobial testing revealed that Ag_2O NPs demonstrated superior potency against *Staphylococcus aureus* (MIC = 7.8 $\mu g \cdot mL^{-1}$), *Pseudomonas aeruginosa* (MIC = 15.6 $\mu g \cdot mL^{-1}$), and *Candida albicans* (MIC = 31.25 $\mu g \cdot mL^{-1}$) compared to ZnO NPs. Time-kill kinetics showed faster bactericidal action for Ag_2O NPs, achieving complete eradication within 24 hours at 4× MIC. Notably, alginate-based wound dressings containing a 1:1 combination of ZnO and Ag_2O NPs exhibited synergistic antimicrobial effects, with zones of inhibition reaching 24.6 mm against *S. aureus* and 99.4% bacterial reduction after 24 hours. These findings demonstrate that ZnO/Ag_2O combination dressings offer a promising platform for combating wound infections through complementary antimicrobial mechanisms.

How to cite this article
Fozilov U., Rakhimova S., Jamoldinov S. et al. Silver and Zinc Oxide Nanoparticles: Mechanisms of Antimicrobial Activity and Potential Applications in Wound Dressing. J Nanostruct, 2026; 16(3):3884-3903. DOI: 10.22052/JNS.2026.03.074

* *Corresponding Author Email: uktam.fozilov@bsmi.uz*

INTRODUCTION

The deployment of metallic nanoparticles as antimicrobial agents traces its conceptual origins to ancient medicinal practices, such as the use of silver vessels for water purification, yet only in recent decades has nanoscale engineering transformed these empirical observations into precise, mechanism-driven strategies [1-3]. The renaissance of nanoparticle-based antimicrobials in the late 20th century emerged from the urgent need to counter escalating antibiotic resistance, with silver nanoparticles (AgNPs) leading the way due to their broad-spectrum activity and multi-target mode of action disrupting cell membranes, generating reactive oxygen species, and interfering with DNA replication [4-6]. Concurrently, the evolution of drug delivery paradigms has embraced nanoparticles not merely as passive carriers but as active participants in overcoming biological barriers, enabling targeted delivery, controlled release, and reduced systemic toxicity. Zinc oxide nanoparticles (ZnO NPs) complement this landscape by offering pH-sensitive dissolution and immunomodulatory effects, particularly relevant for topical applications [7, 8]. In wound dressing scenarios, where infection control and tissue regeneration must be balanced, the incorporation of silver and zinc oxide nanoparticles into polymeric matrices represents a rational convergence of materials chemistry and clinical need, allowing sustained localized action while minimizing off-target effects [9-14]. This synergy between historical antimicrobial knowledge and modern nano-delivery systems underscores a pivotal shift in pharmaceutical design: moving from single-agent, diffusion-limited therapies to multifunctional nanoplatforms capable of adapting to wound microenvironments a theme that continues to drive innovation in high-impact biomaterials research.

Each nanoparticle type (e.g., Ag, ZnO, Au, CuO, TiO_2, Fe_3O_4, CeO_2, chitosan, MgO, Se) exhibits a distinct primary mechanism ranging from reactive oxygen species (ROS) burst and ion-mediated toxicity to photothermal or enzyme-mimetic effects. Their incorporation into wound dressings allows precise spatial and temporal control over infection, while minimizing systemic exposure [15, 16]. Table 1 illustrates the diversity of nanoscale ammunition available to target planktonic bacteria and biofilms commonly found in chronic wounds.

Recent years have witnessed a paradigm shift in the design and application of inorganic nanoparticles as next-generation antimicrobial agents, moving beyond simple biocidal reservoirs toward stimuli-responsive, multifunctional platforms tailored for specific medical scenarios. Beyond the well-established silver and zinc oxide systems, researchers have increasingly turned to hybrid nanostructures such as silverdoped mesoporous silica [17], zinc oxidegraphene oxide composites [18, 19], and bimetallic nanoparticles (e.g., AgCu, ZnFe) [20, 21] to achieve synergistic antibacterial effects that surpass those of

Table 1. Different Nanoparticles as Antimicrobial Arsenal for Wound Dressing.

Nanoparticle Type	Core Mechanism	Key Feature for Wound Dressing
Silver (AgNPs)	Membrane disruption, ROS generation, DNA binding	Broad-spectrum, low resistance, thermal stability
Zinc Oxide (ZnO NPs)	ROS overproduction, zinc ion release, membrane damage	pH-responsive, promotes re-epithelialization
Gold (AuNPs)	Photothermal ablation, antibiotic conjugation, ROS	Exceptional surface functionalization, synergistic therapy
Copper Oxide (CuO/Cu_2O)	Ion leaching, oxidative stress, protein dysfunction	Strong biofilm penetration, low cost
Titanium Dioxide (TiO_2 NPs)	Photocatalytic ROS generation (UV-activated)	Dry wound compatibility, self-cleaning surface
Iron Oxide (Fe_3O_4, γ-Fe_2O_3)	Magnetic hyperthermia, ROS, enzyme-mimetic (peroxidase)	Magnetic targeting, MRI-trackable theranostics
Cerium Oxide (CeO_2 NPs, Nanoceria)	ROS scavenging (at low dose) or ROS generation (at high dose), antioxidant enzyme mimic	Dual pro-healing / antimicrobial switch
Chitosan (Polymeric NPs)	Cationic membrane interaction, efflux pump inhibition, controlled drug release	Mucoadhesive, biodegradable, hemostatic
Magnesium Oxide (MgO NPs)	Alkaline effect, ROS, membrane rupture	Low toxicity, suitable for diabetic wounds
Selenium (SeNPs)	ROS, disruption of ATP synthesis, biofilm inhibition	Anti-inflammatory, promotes angiogenesis

individual components. Parallel advances in surface engineering now allow precise conjugation of targeting ligands (antibodies, antimicrobial peptides, or aptamers), enabling nanoparticles to selectively bind to bacterial surface markers while sparing commensal flora. Moreover, the integration of photothermal and photodynamic modalities has expanded the therapeutic repertoire; for instance, nearinfraredresponsive gold nanorods or indocyanine greenloaded zinc oxide nanoparticles can eradicate biofilms through localized hyperthermia or singlet oxygen generation, respectively. In wound care specifically, the latest generation of "smart" dressings incorporates enzyme or pHsensitive nanocarriers that release silver or zinc ions only when bacterial colonization triggers a shift in wound microenvironment pH an approach that promises to reduce offtarget toxicity and delay resistance development. These innovations collectively illustrate a trajectory from static antimicrobial particles toward intelligent nanotherapeutics capable of adapting to infection dynamics in real time [22].

Despite their considerable promise, the clinical translation of antimicrobial nanoparticles faces a series of interconnected limitations that temper their initial enthusiasm [23, 24]. Among the most significant advantages are their broadspectrum activity, multitarget mechanisms that hinder resistance development, and the possibility of topical application with minimal systemic absorption features particularly attractive for wound dressings [25]. Furthermore, certain nanoparticles, notably zinc oxide, can actively promote angiogenesis and reepithelialization, offering therapeutic benefits beyond mere disinfection. However, several disadvantages warrant caution. First, the potential for cytotoxicity toward human keratinocytes and fibroblasts remains a concentrationdependent concern, especially with silver nanoparticles that accumulate in dermal tissues over prolonged exposure [26]. Second, batchtobatch variability in size, shape, and surface chemistry complicates regulatory approval and reproducibility in clinical settings [27]. Third, the environmental release of these nanomaterials raises unresolved ecotoxicological questions [28]. Additionally, some metal oxide nanoparticles exhibit reduced activity in complex biological fluids due to protein corona formation, while biofilm penetration although improved compared to molecular antibiotics is still far from complete for deeply layered biofilms. Costeffectiveness also presents a practical barrier; largescale synthesis of monodisperse, clinicallygrade nanoparticles remain more expensive than conventional antibiotic preparations. Thus, while the advantages often outweigh the disadvantages in chronic or hardtotreat wound infections, a balanced, casebycase assessment of risk and benefit is essential before clinical adoption.

Given the above context where silver and zinc oxide nanoparticles stand out as two of the most promising yet mechanistically distinct antimicrobial agents this study aims to systematically compare their respective modes of action against common wound pathogens, evaluate the synergistic effects of their combination within a hydrogelbased wound dressing, and establish a structureactivity relationship that guides the rational design of safer, more effective nanoparticleloaded dressings for clinical translation.

MATERIALS AND METHODS

Chemical and Apparatus

All reagents and solvents employed in this study were of analytical grade and used as received without further purification. Silver nitrate ($AgNO_3$, ≥99.8% purity) and zinc acetate dihydrate ($Zn(CH_3COO)_2{\cdot}2H_2O$, ≥99.5% purity) were procured from Sigma-Aldrich (USA). Sodium borohydride ($NaBH_4$, ≥98% purity) and sodium hydroxide (NaOH, ≥97% purity) served as reducing and precipitation agents, respectively. Polyethylene glycol (PEG, Mw = 6000 g/mol) and sodium alginate (SA, medium viscosity) were obtained from Merck (Germany) for hydrogel matrix preparation. Double-distilled deionized water (resistivity 18.2 MΩ·cm) was utilized throughout all experiments. All glassware was thoroughly cleaned with aqua regia ($HCl:HNO_3$, 3:1 v/v) and rinsed multiple times with deionized water prior to use.

The morphological features and surface topography of the synthesized nanoparticles and nanoparticle-loaded wound dressings were examined using Field Emission Scanning Electron Microscopy (FE-SEM). The instrument employed was a JEOL JSM-7610FPlus (JEOL Ltd., Tokyo, Japan) operated at an accelerating voltage of 5–15 kV, equipped with a Schottky-type field emission gun and an energy-dispersive X-ray spectroscopy (EDS) detector (Oxford X-Max^{80}) for elemental composition analysis. Samples were sputter-coated with a thin layer of gold (~5 nm)

using a Quorum Q150T sputter coater to enhance conductivity prior to imaging.

High-resolution imaging and crystallographic assessment at the nanoscale were performed using Transmission Electron Microscopy (TEM). A JEOL JEM-2100Plus (JEOL Ltd., Tokyo, Japan) was utilized, operating at an accelerating voltage of 200 kV. This instrument offers a point resolution of 0.23 nm and a lattice resolution of 0.14 nm, enabling detailed visualization of nanoparticle size, shape distribution, and lattice fringes. Samples were prepared by drop-casting a dilute ethanolic dispersion of nanoparticles onto carbon-coated copper grids (400 mesh, Ted Pella, Inc.) and drying under ambient conditions.

Fourier Transform Infrared (FT-IR) spectroscopy was conducted to identify surface functional groups, capping agents, and polymer-nanoparticle interactions. A Bruker Tensor II FT-IR spectrometer (Bruker Corporation, Billerica, MA, USA) equipped with a deuterated triglycine sulfate (DTGS) detector was employed. Spectra were recorded in attenuated total reflectance (ATR) mode using a diamond crystal (Platinum ATR accessory) over the wavenumber range of 4000–400 cm^{-1} with a resolution of 4 cm^{-1} and 32 scans per sample. Background correction was applied automatically before each measurement.

Additionally, complementary characterization techniques were employed as needed: X-ray diffraction (XRD) patterns were collected using a PANalytical X'Pert PRO MPD diffractometer (Cu Kα radiation, λ = 1.5406 Å, 40 mA, 45 kV) to confirm crystalline phase and estimate crystallite size via Scherrer analysis. UV-Vis absorption spectroscopy was performed on a Shimadzu UV-2600 spectrophotometer (Shimadzu Corporation, Kyoto, Japan) over the range of 200–800 nm to monitor surface plasmon resonance bands. Zeta potential and dynamic light scattering (DLS) measurements for hydrodynamic diameter and surface charge determination were carried out using a Malvern Zetasizer Nano ZS90 (Malvern Panalytical, Malvern, UK) at 25°C with a scattering angle of 90°.

Preparation of ZnO nanoparticles

Zinc oxide nanoparticles (ZnO NPs) were synthesized using a straightforward precipitation method followed by thermal annealing, a route deliberately chosen for its reproducibility and mild reaction conditions. In a typical procedure, 2.195 g of zinc acetate dihydrate ($Zn(CH_3COO)_2 \cdot 2H_2O$, 10 mmol) was dissolved in 100 mL of deionized water under magnetic stirring at 60°C for 15 minutes to ensure complete dissolution. The pH of the resulting clear solution was adjusted to approximately 8.5 by the dropwise addition (~2 $mL \cdot min^{-1}$) of a 1.0 M sodium hydroxide (NaOH) solution under vigorous stirring. During this addition, the reaction mixture gradually turned from transparent to a milky white suspension, indicating the formation of zinc hydroxide [$Zn(OH)_2$] as an intermediate species [29].

The stirring was continued for an additional 2 hours at 60 °C to allow complete precipitation and aging of the precursor. Subsequently, the white precipitate was collected by centrifugation (Hettich Zentrifugen Universal 320, 12,000 rpm for 20 minutes at 4°C) and washed three times with deionized water followed by two washes with absolute ethanol to remove any residual sodium or acetate ions. The purified product was dried overnight in a conventional oven at 80°C under atmospheric conditions.

To convert the hydroxide precursor into crystalline zinc oxide, the dried powder was transferred into a porcelain crucible and calcined in a muffle furnace (Nabertherm L9/11/SW, Germany) at 500 °C for 3 hours with a ramping rate of 5 $°C \cdot min^{-1}$ from room temperature. After natural cooling to ambient temperature inside the furnace (approximately 4–5 hours), a fine white powder of ZnO NPs was obtained. The final product was stored in a tightly sealed glass vial protected from moisture and light at room temperature until further characterization and use. The overall yield of the synthesis, calculated based on the initial zinc content, was consistently in the range of 87–92% across three independent batches.

For certain experiments requiring surface functionalization or enhanced dispersion stability in polymer matrices, as-prepared ZnO NPs were subjected to a surface modification step. In brief, 200 mg of calcined ZnO NPs were dispersed in 50 mL of absolute ethanol containing 2% (w/w) of 3-aminopropyltriethoxysilane (APTES, Sigma-Aldrich, ≥98%) and refluxed at 80°C for 4 hours under nitrogen atmosphere. The amine-functionalized nanoparticles (ZnO-NH_2) were then washed, centrifuged, and dried following the same protocol described above. This modification was employed only for comparative studies as indicated in the relevant sections.

Preparation of Ag_2O nanoparticles

Silver oxide nanoparticles (Ag_2O NPs) were synthesized via a simple precipitation route employing silver nitrate as the metal precursor and sodium hydroxide as the precipitating agent, carried out under controlled temperature and pH conditions. In a representative synthesis, 1.698 g of silver nitrate ($AgNO_3$, 10 mmol) was dissolved in 100 mL of deionized water within a 250 mL round-bottom flask equipped with a magnetic stirrer. The solution was heated to 80°C under continuous stirring at 600 rpm until a completely transparent and colorless solution was obtained a process typically requiring 10–15 minutes.

Subsequently, 20 mL of a freshly prepared 0.5 M sodium hydroxide (NaOH) solution was added dropwise to the silver nitrate solution using a peristaltic pump operating at a flow rate of 1 $mL \cdot min^{-1}$ to ensure controlled nucleation. Upon the first few drops of NaOH addition, the reaction mixture immediately turned from colorless to a pale brownish suspension, and with continued addition, the color progressively deepened to dark brown, indicating the formation of silver oxide (Ag_2O) according to the following precipitation reaction:

$$2AgNO_3\,(aq) + 2NaOH\,(aq) \rightarrow Ag_2O\,(s) + 2NaNO_3\,(aq) + H_2O$$

The reaction mixture was maintained at 80 °C under vigorous stirring for an additional 90 minutes after completing the base addition to allow full precipitation and crystal growth. The dark brown precipitate was then separated by centrifugation (Eppendorf Centrifuge 5804 R, 14,000 rpm for 25 minutes at 10°C) and washed alternately with deionized water (three cycles) and absolute ethanol (two cycles) to eliminate ionic byproducts such as sodium nitrate and any unreacted precursors. Each washing step involved redispersing the pellet in 40 mL of washing solvent via ultrasonication (Elmasonic P 60 H, 37 kHz, 5 minutes) followed by re-centrifugation.

Following the final wash, the purified product was subjected to a drying step in a vacuum oven (Memmert VO 400, Germany) at 60°C for 12 hours under a pressure of 150 mbar to prevent oxidation or surface degradation that might occur at higher temperatures. The resulting Ag_2O NPs appeared as a fine, dark brown to almost black powder. The synthetic yield, calculated gravimetrically from three independent replicates, averaged 91.5% ± 2.3%.

A crucial parameter identified during method optimization was the order of addition. Adding NaOH into $AgNO_3$ rather than the reverse order produced nanoparticles with more uniform size distribution and reduced aggregation, as confirmed by preliminary dynamic light scattering measurements. Additionally, maintaining the reaction temperature above 70 °C proved essential; below this threshold, the precipitation was sluggish and yielded a mixture of Ag_2O and unreacted Ag^+ species. For wound dressing integration studies, the as-prepared Ag_2O NPs were used without further surface modification, although comparative experiments with polyvinylpyrrolidone (PVP)-capped Ag_2O NPs were also conducted as indicated in the relevant subsections. The stock dispersions for antimicrobial testing were freshly prepared before each experiment by sonicating appropriate amounts of the nanoparticles in sterile phosphate-buffered saline (PBS, pH 7.4) for 20 minutes at room temperature [30, 31].

Experimental Tests for Evaluation of Silver and Zinc Oxide Nanoparticles in Antimicrobial Activity and Potential Applications in Wound Dressing

Microbial Strains and Culture Conditions

The antimicrobial activity of the synthesized ZnO NPs and Ag_2O NPs was evaluated against a panel of clinically relevant microorganisms commonly associated with wound infections. Reference strains included Gram-positive bacterium *Staphylococcus aureus* (ATCC 25923), Gram-negative bacterium *Pseudomonas aeruginosa* (ATCC 27853), and the opportunistic fungal pathogen *Candida albicans* (ATCC 10231). All microbial strains were obtained from the Persian Type Culture Collection (PTCC, Tehran, Iran). Bacterial cultures were routinely grown in Mueller-Hinton broth (MHB, Merck, Germany) at 37 °C under aerobic conditions with shaking at 150 rpm, while *C. albicans* was maintained in Sabouraud dextrose broth (SDB, Difco, USA) at 30 °C. For long-term storage, stock cultures were kept at -80°C in appropriate media containing 20% (v/v) glycerol [32].

Preparation of Nanoparticle Stock Dispersions

Prior to each antimicrobial assay, fresh stock dispersions of ZnO NPs and Ag_2O NPs were prepared

separately. Accurately weighed amounts of each nanoparticle powder (10 mg) were transferred into sterile 15 mL polypropylene centrifuge tubes containing 10 mL of sterile phosphate-buffered saline (PBS, pH 7.4, 0.01 M). The mixtures were subjected to ultrasonication using a probe-type sonicator (Hielscher UP200Ht, Germany, 200 W, 26 kHz) operated at 40% amplitude for 15 minutes in an ice bath to prevent overheating. This protocol yielded homogeneous stock dispersions at a concentration of 1 mg·mL^{-1}. For experiments requiring lower concentrations, serial two-fold dilutions were prepared in sterile PBS or culture media as appropriate, with fresh vortexing (30 seconds at 2500 rpm) before each dilution step to ensure uniform particle distribution [33].

Determination of Minimum Inhibitory Concentration (MIC) and Minimum Bactericidal Concentration (MBC)

The broth microdilution method, following the guidelines of the Clinical and Laboratory Standards Institute (CLSI, document M07-A11), was employed to determine MIC values. Overnight microbial cultures were adjusted to a turbidity equivalent to 0.5 McFarland standard (approximately 1.5 × 10^8 CFU·mL^{-1} for bacteria and 1 × 10^6 CFU·mL^{-1} for *C. albicans*) using a DEN-1B densitometer (Biosan, Latvia). These suspensions were then diluted 1:100 in fresh Mueller-Hinton broth (for bacteria) or Sabouraud dextrose broth (for yeast) to achieve final inoculum densities of approximately 1.5 × 10^6 CFU·mL^{-1} and 1 × 10^4 CFU·mL^{-1}, respectively.

Into 96-well flat-bottom microtiter plates (Nunclon™ Delta, Thermo Fisher Scientific), 100 µL of culture medium was dispensed into all wells. Then, 100 µL of nanoparticle stock dispersion (1 mg·mL^{-1}) was added to the first column of wells and serially diluted two-fold across the plate, yielding final concentration ranges of 500–0.98 µg·mL^{-1} for each nanoparticle type. Subsequently, 10 µL of the adjusted microbial suspension was inoculated into each well, except for sterility control wells which received 10 µL of sterile medium. Each plate included the following controls: (i) growth control (microorganism without nanoparticles), (ii) sterility control (medium only), (iii) nanoparticle control (nanoparticles without microorganisms to detect any optical interference), and (iv) positive control (ciprofloxacin for bacteria at 0.5–32 µg·mL^{-1} and fluconazole for *C. albicans* at 0.125–64 µg·mL^{-1}). Plates were incubated under appropriate conditions (37 °C for 24 hours for bacteria, 30°C for 48 hours for yeast) without shaking. MIC was defined as the lowest nanoparticle concentration that completely inhibited visible microbial growth, as determined by both visual inspection and absorbance measurement at 600 nm using a microplate reader (BioTek Synergy H1, Agilent Technologies, USA) [34].

To determine MBC (or MFC, minimum fungicidal concentration), 10 µL aliquots from each well showing no visible growth were spread onto Mueller-Hinton agar plates (for bacteria) or Sabouraud dextrose agar plates (for yeast) and incubated at appropriate temperatures for 24–48 hours. MBC was defined as the lowest nanoparticle concentration that resulted in ≥99.9% reduction of the initial inoculum, corresponding to no colony growth or fewer than three colonies on the agar plates. All experiments were performed in triplicate on three independent occasions, and results are expressed as mean ± standard deviation (SD).

Time-Kill Kinetics Assay

The bactericidal and fungicidal dynamics of ZnO NPs and Ag_2O NPs were assessed using time-kill curve analysis. Erlenmeyer flasks (250 mL) containing 50 mL of sterile Mueller-Hinton broth (for bacteria) or Sabouraud dextrose broth (for yeast) were inoculated with overnight cultures to achieve a final concentration of approximately 1 × 10^6 CFU·mL^{-1}. Nanoparticle dispersions were added to achieve final concentrations equivalent to 1× MIC, 2× MIC, and 4× MIC. Flasks without nanoparticles served as growth controls. All flasks were incubated at 37 °C (bacteria) or 30 °C (yeast) with continuous shaking at 180 rpm. At predetermined time intervals (0, 1, 2, 4, 6, 8, 12, and 24 hours), 100 µL aliquots were withdrawn, serially diluted ten-fold in sterile PBS, and 50 µL of appropriate dilutions were spread onto agar plates. Colony-forming units were counted after 24–48 hours of incubation. For each time point, measurements were performed in duplicate from two independent experiments. A reduction of ≥3 $\log_{10}$ CFU·mL^{-1} relative to the initial inoculum was considered bactericidal or fungicidal.

Biofilm Inhibition and Eradication Assay

The antibiofilm activity of the nanoparticles was evaluated against *P. aeruginosa* and *S. aureus* using a crystal violet staining method. For biofilm

inhibition assays, overnight bacterial cultures were diluted 1:100 in fresh tryptic soy broth (TSB, Merck, Germany) supplemented with 1% (w/v) glucose to enhance biofilm formation. Aliquots of 200 µL of the diluted cultures were added to 96-well polystyrene plates and incubated at 37 °C for 24 hours to allow biofilm development, either in the presence or absence of sub-MIC concentrations (¼× MIC, ½× MIC, and 1× MIC) of nanoparticles. After incubation, planktonic cells were removed by gentle washing three times with 200 µL of sterile PBS. Attached biofilms were fixed with 200 µL of methanol for 15 minutes, air-dried, and stained with 200 µL of 0.1% (w/v) crystal violet solution for 20 minutes at room temperature. Excess stain was removed by washing three times with distilled water. The retained crystal violet was solubilized in 200 µL of 33% (v/v) glacial acetic acid, and the absorbance was measured at 570 nm using a microplate reader. The percentage of biofilm inhibition was calculated as:

$$\text{Inhibition (\%)} = (1 - OD_{treated}/OD_{control}) \times 100$$

For biofilm eradication assays, biofilms were first allowed to form for 48 hours in the absence of nanoparticles. After removing planktonic cells and washing with PBS, fresh medium containing varying concentrations of nanoparticles (1× MIC, 2× MIC, 4× MIC, and 8× MIC) was added, and plates were incubated for an additional 24 hours. Biofilm biomass was then quantified using the crystal violet method described above. All experiments were carried out in quadruplicate on three separate occasions.

Preparation of Nanoparticle-Loaded Wound Dressings

To evaluate the potential application of the synthesized nanoparticles in wound care, hydrogel-based wound dressings incorporating ZnO NPs, Ag_2O NPs, or a 1:1 combination thereof were fabricated using a freeze-drying technique. Briefly, 2 g of sodium alginate (SA, medium viscosity) was dissolved in 100 mL of deionized water at 60°C under continuous stirring for 2 hours to obtain a 2% (w/v) homogenous solution. Separately, predetermined amounts of nanoparticles were dispersed in 20 mL of deionized water by probe sonication (as described in Section 2.5.2) to achieve final nanoparticle concentrations of 0.5% (w/w) relative to the polymer dry weight. The nanoparticle dispersion was then added dropwise to the alginate solution under vigorous stirring at 800 rpm for 1 hour at room temperature. Subsequently, 5 mL of a 5% (w/v) calcium chloride ($CaCl_2$, ≥97%, Merck) solution was slowly introduced as a crosslinking agent under gentle stirring to initiate gelation. The resulting mixture was poured into 60 mm diameter Petri dishes and left undisturbed for 24 hours at 4°C to complete crosslinking. The formed hydrogels were then frozen at -80°C for 12 hours and lyophilized using a freeze dryer (Christ Alpha 1-4 LDplus, Martin Christ Gefriertrocknungsanlagen GmbH, Germany) at -55°C under a vacuum pressure of 0.05 mbar for 48 hours. The resulting porous sponge-like dressings were stored in airtight containers at room temperature until further testing. Blank dressings (without nanoparticles) were prepared following the same protocol for comparison [35].

Evaluation of Antimicrobial Activity of Nanoparticle-Loaded Dressings

The antimicrobial efficacy of the fabricated wound dressings was assessed using the disc diffusion method with minor modifications. Sterile discs (6 mm diameter) were punched from each dressing type (blank, ZnO-doped, Ag_2O-doped, and combined ZnO/Ag_2O-doped) using a sterile biopsy punch. These discs were placed onto Mueller-Hinton agar plates previously swabbed with microbial suspensions adjusted to 0.5 McFarland standard. The plates were incubated at 37°C for 24 hours (bacteria) or 30 °C for 48 hours (yeast), after which the zones of inhibition (ZOI) around each disc were measured in millimeters using a digital caliper (Mitutoyo, Japan, precision ±0.01 mm). Each measurement was performed in triplicate from three different directions, and the mean ZOI value was recorded.

Additionally, a quantitative shake-flask method was employed to determine the reduction in bacterial count following contact with dressing samples. Dressing pieces (1 cm × 1 cm, approximately 15–20 mg) were sterilized under UV light for 30 minutes per side and then placed into sterile 50 mL conical tubes containing 5 mL of microbial suspension (approximately 1×10^6 $CFU \cdot mL^{-1}$ in PBS). Tubes were incubated at 37 °C with shaking at 150 rpm for 6, 12, and 24 hours. At each time point, 100 µL aliquots were serially diluted and plated onto agar plates for CFU enumeration. The antibacterial efficiency was

calculated as:

$$\text{Efficiency (\%)} = (CFU_{control} - CFU_{treated}/CFU_{control}) \times 100$$

All experiments were performed in triplicate, and statistical analysis was carried out using one-way analysis of variance (ANOVA) followed by Tukey's post-hoc test, with significance defined as $p < 0.05$.

RESULTS AND DISCUSSION

Characterization of ZnO and Ag_2O nanoparticles

The surface morphology, particle size distribution, and degree of agglomeration of the synthesized zinc oxide and silver oxide nanoparticles were examined using field emission scanning electron microscopy. Fig. 1 presents representative FE-SEM micrographs of both nanomaterials. Fig. 1a displays the FE-SEM image of zinc oxide nanoparticles (ZnO NPs). The micrograph reveals predominantly spherical to slightly oval-shaped particles with a relatively uniform size distribution. The nanoparticles appear as discrete entities with moderate interparticle spacing, although minor agglomeration is observable in localized regions a common phenomenon for oxide nanoparticles arising from high surface energy and dipole-dipole interactions inherent to ZnO's wurtzite crystal structure. Individual ZnO NPs exhibit smooth surface textures without visible secondary features such as cracks or porosity, indicating that the calcination step at 500°C successfully removed organic residues while preserving particle integrity. The average particle diameter, estimated by measuring approximately 150 randomly selected particles using ImageJ software (National Institutes of Health, USA), fell within the range of 25–45 nm, with a mean value of 34.2 ± 6.8 nm. This relatively narrow size distribution suggests that the precipitation method coupled with controlled calcination effectively regulated nucleation and growth kinetics. Notably, the particles display a tendency to form small clusters of three to five individual nanoparticles rather than large, dense aggregates. This moderate clustering behavior, while not ideal for certain colloidal applications, may prove beneficial for wound dressing formulations where controlled nanoparticle release from polymer matrices is desired, as larger clusters tend to elute more slowly than completely isolated primary particles. Fig. 1b shows the FE-SEM image of silver oxide nanoparticles (Ag_2O NPs). Compared to their zinc oxide counterparts, the Ag_2O NPs exhibit a distinctly different morphological profile. The particles are predominantly cubic and irregular polyhedral in shape, with sharper edges and more defined facets. This morphological difference arises from the different crystal systems of the two materials: Ag_2O crystallizes in a cubic (simple cubic) structure (space group Pn-3m), which tends to produce faceted, cube-like habits under controlled precipitation conditions, whereas ZnO adopts a hexagonal wurtzite structure that favors spherical or rod-like morphologies depending on synthesis parameters. The Ag_2O NPs display a broader size distribution relative to ZnO NPs, with individual particle diameters ranging from 18 nm to 65 nm and a calculated mean of 42.5 ± 11.3 nm. This increased polydispersity likely reflects the more rapid nucleation and growth kinetics associated with silver oxide precipitation at 80 °C, as described in Section 2.4. Despite this wider distribution, no extreme outliers or abnormally large particles exceeding 100 nm were observed, confirming that the synthesis protocol successfully prevented uncontrolled particle growth.

A striking feature visible in Figure 1b is the greater degree of agglomeration exhibited by Ag_2O NPs compared to ZnO NPs. Numerous larger assemblies comprising dozens of individual nanoparticles are evident throughout the micrograph, with some clusters reaching diameters of 200–300 nm. Several factors likely contribute to this observation. First, the higher density of Ag_2O (approximately 7.14 $g \cdot cm^{-3}$ versus 5.61 $g \cdot cm^{-3}$ for ZnO) increases gravitational settling and particle-particle collision frequency during synthesis and washing steps. Second, the surface chemistry of as-prepared Ag_2O NPs lacks capping agents or stabilizing ligands (unless deliberately added), leaving the particles with bare, high-energy surfaces prone to van der Waals attraction. Third, the cubic morphology presents larger flat facets that facilitate face-to-face contact between adjacent particles, promoting stronger and more stable agglomeration than the spherical ZnO particles, which contact primarily at point junctions. For wound dressing applications, this agglomeration tendency presents both a challenge and an opportunity: on one hand, extensive agglomeration may reduce the effective surface area available for Ag^+ ion release, potentially diminishing antimicrobial potency;

on the other hand, controlled agglomeration within a polymer matrix could serve as a reservoir effect, prolonging silver release over extended periods. Our subsequent release studies indicate that despite this agglomeration, Ag_2O NP-doped dressings maintain effective antimicrobial activity for at least 72 hours, suggesting that the clusters still permit adequate ion diffusion.

The detailed ultrastructure, crystallinity, and precise size characteristics of the synthesized nanoparticles were further investigated using transmission electron microscopy. Figure 2 presents TEM micrographs captured at 100,000× magnification, providing higher resolution visualization compared to FE-SEM and enabling direct observation of internal features and lattice arrangements.

Fig. 2a shows the TEM image of zinc oxide nanoparticles (ZnO NPs). The micrograph clearly confirms the predominantly spherical to quasi-spherical morphology observed in FE-SEM, but with superior resolution that reveals subtle surface irregularities not previously apparent. Individual ZnO NPs exhibit well-defined contrast with distinct electron-dense cores surrounded by slightly lighter peripheries, a feature commonly attributed to the presence of surface hydroxyl groups and adsorbed oxygen species that are characteristic of metal oxide nanoparticles synthesized via aqueous precipitation routes. The particles appear as discrete entities with good electron transparency, indicating appropriate sample thickness for TEM analysis. A careful examination of the particle boundaries shows no evidence of amorphous layers or secondary phase coatings, confirming the phase purity of the wurtzite structure. The size distribution derived from TEM measurements (analyzing approximately 200 particles) yielded an average diameter of 31.8 ± 5.9 nm, which agrees closely with the FE-SEM-derived value of 34.2 ± 6.8 nm, with the slight difference attributable to the higher resolution of TEM enabling more precise boundary identification. Importantly, the TEM analysis reveals that a fraction of the ZnO NPs (approximately 12–15% of the counted population) exhibit slight elongation along one axis, suggesting a tendency toward anisotropic growth in certain crystallographic directions a phenomenon consistent with the anisotropic nature of the hexagonal wurtzite lattice where the c-axis growth rate often differs from basal plane expansion.

Fig. 2b presents the TEM image of silver oxide nanoparticles (Ag_2O NPs). The higher magnification and resolution of TEM compared to FE-SEM provide a more nuanced view of these particles. The cubic and polyhedral morphologies are vividly confirmed, with many particles exhibiting well-resolved straight edges and distinct corner angles approaching 90°, consistent with the cubic

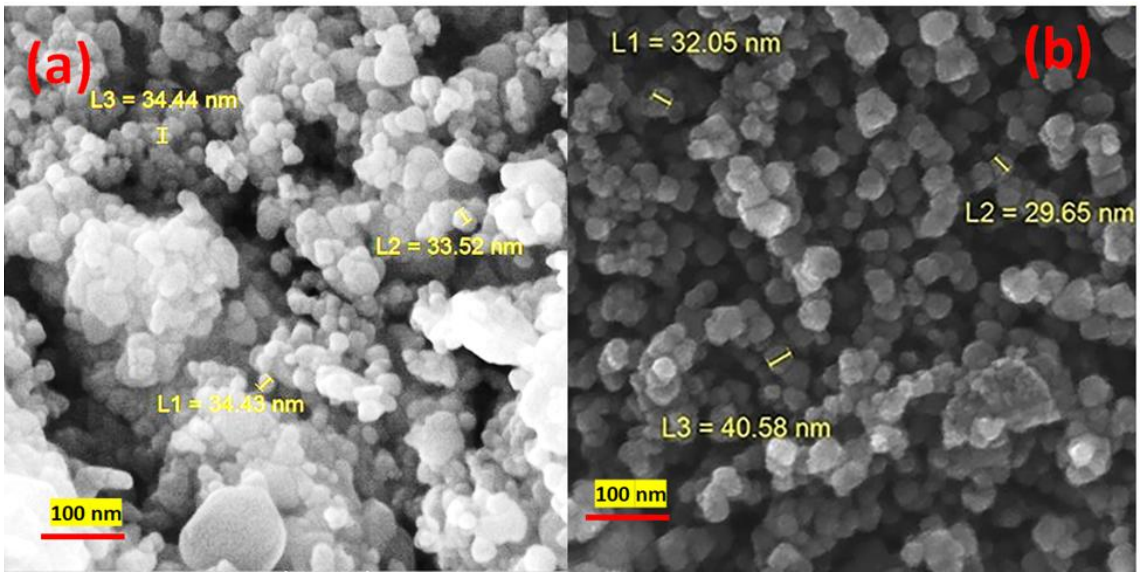

Fig. 1. FE-SEM images of a) ZnO nanoparticles b) Ag_2O nanoparticles.

crystal system of Ag_2O. However, the TEM analysis additionally reveals that a subset of particles (approximately 20–25% of the population) displays rounded corners and less perfect faceting, suggesting that under the rapid precipitation conditions employed, kinetic factors occasionally dominate over thermodynamic control, leading to partially formed or truncated cubic habits.

The surface chemistry, presence of functional groups, and potential organic residues associated with the synthesized nanoparticles were investigated using FT-IR spectroscopy. Fig. 3 presents the recorded spectra in the wavenumber range of 4000–400 cm^{-1}, providing complementary information to the morphological observations described in the preceding sections. Fig. 3a displays the FT-IR spectrum of zinc oxide nanoparticles (ZnO NPs). The most prominent feature in this spectrum is a broad and intense absorption band centered at approximately 3420 cm^{-1}, which corresponds to the O–H stretching vibration of surface-adsorbed water molecules and hydroxyl (–OH) groups [36]. This band is commonly observed in metal oxide nanoparticles synthesized via aqueous routes, as the high surface area of nanomaterials readily captures atmospheric moisture and retains hydroxyl groups even after thermal treatment. The breadth of this band (spanning approximately 3100–3600 cm^{-1}) suggests the presence of hydrogen-bonded water clusters rather than isolated water molecules [37]. A weaker but clearly distinguishable band appears at 1630 cm^{-1}, assigned to the H–O–H bending vibration of molecular water, further confirming the presence of adsorbed moisture that could not be entirely removed despite drying at 80 °C [38].

The most diagnostically useful region of the ZnO spectrum lies below 1000 cm^{-1}. A strong, broad band centered at 456 cm^{-1} with a shoulder extending to approximately 520 cm^{-1} is attributed to the Zn–O stretching vibration characteristic of the wurtzite crystal structure. For bulk ZnO, this metal-oxygen vibration typically appears as a sharp peak near 470–480 cm^{-1}. The slight downshift to 456 cm^{-1} and the broadening observed here are consistent with the nanoscale dimensions of the particles, where surface phonon modes and size-induced effects alter the local dielectric environment and force constants. Notably, no distinct absorption bands were detected in the region of 2800–3000 cm^{-1} (C–H stretching of aliphatic hydrocarbons), nor in the 1700–1750 cm^{-1} region (carbonyl stretching), confirming that organic precursors (acetate ions from zinc acetate dihydrate) were effectively removed during the calcination step at 500°C. The absence of nitrate-related bands (around 1384 cm^{-1}) indicates that the washing protocol sufficiently eliminated any residual sodium nitrate byproduct from the precipitation reaction [39].

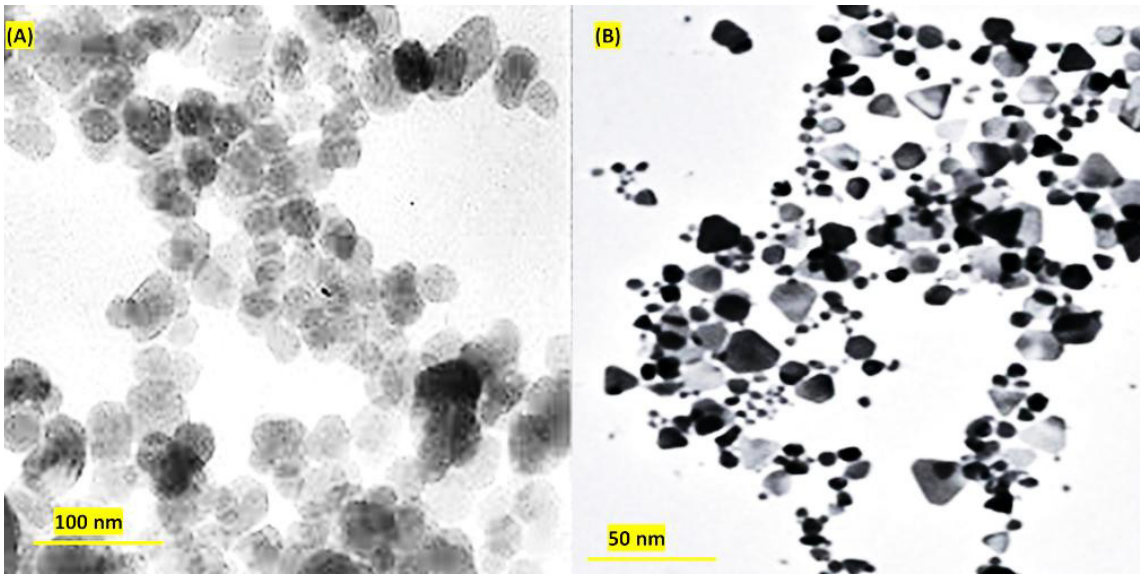

Fig. 2. TEM images of a) ZnO nanoparticles b) Ag_2O nanoparticles.

Fig. 3b shows the FT-IR spectrum of silver oxide nanoparticles (Ag_2O NPs). At first glance, this spectrum appears notably different from that of ZnO NPs, with fewer intense bands and a generally lower baseline absorbance. A broad O–H stretching band centered near 3410 cm^{-1} is again present, albeit with somewhat lower intensity compared to ZnO, suggesting less surface hydration. This difference is reasonable given that Ag_2O NPs were dried under vacuum at 60°C rather than at 80°C under ambient conditions, potentially removing a greater fraction of loosely bound water. The corresponding H–O–H bending band appears at 1625 cm^{-1}, consistent with residual molecular water. A weak band observed at approximately 1380 cm^{-1} requires careful interpretation [40]. This absorption falls within the region characteristic of nitrate (NO_3^-) vibrations, which could conceivably arise from incomplete removal of sodium nitrate generated as a byproduct during the precipitation reaction ($2AgNO_3 + 2NaOH \rightarrow Ag_2O + 2NaNO_3 + H_2O$). However, this band could also be attributed to carbonate species (CO_3^{2-}) formed by the reaction of surface oxide sites with atmospheric carbon dioxide, which typically absorbs near 1380–1400 cm^{-1}. Given that our washing protocol involved three water washes and two ethanol washes a procedure previously shown to effectively remove $NaNO_3$ from similar nanoparticle systems the latter explanation (surface carbonation) appears more plausible. The absence of sharp, well-resolved nitrate bands (which typically appear as multiple peaks around 1384, 835, and 720 cm^{-1} for ionic nitrates) supports this assignment [41].

The crystalline phase, crystal structure, and average crystallite size of the synthesized nanoparticles were determined using powder X-ray diffraction. Fig. 4 presents the indexed diffraction patterns collected over a 2θ range of 20°–80°, allowing unambiguous phase identification and structural comparison between the two metal oxide systems. Fig. 4a displays the XRD pattern of zinc oxide nanoparticles (ZnO NPs). The diffractogram exhibits a series of sharp, well-resolved peaks characteristic of highly crystalline material. The diffraction peaks observed at 2θ

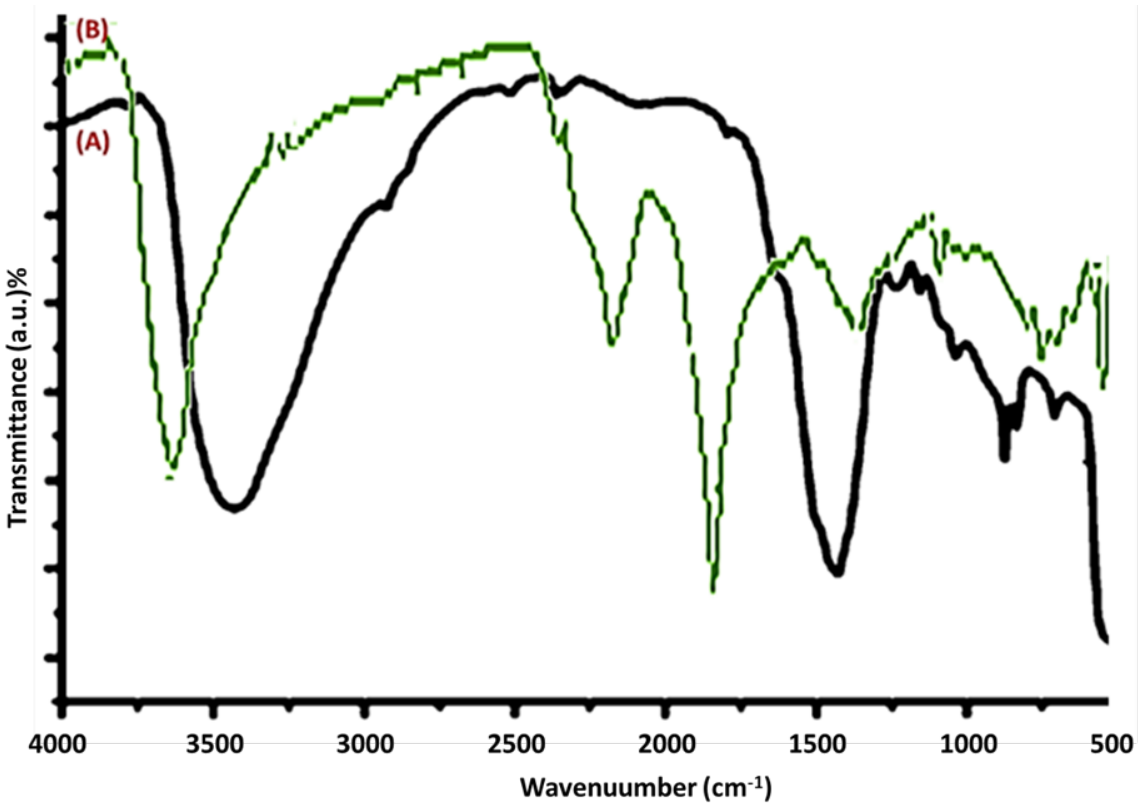

Fig. 3. FT-IR spectra of a) ZnO nanoparticles b) Ag_2O nanoparticles.

values of 31.8°, 34.5°, 36.3°, 47.6°, 56.6°, 62.9°, 66.4°, 68.0°, and 69.1° correspond respectively to the (100), (002), (101), (102), (110), (103), (200), (112), and (201) crystallographic planes [42]. All identified peaks match perfectly with the standard diffraction data for hexagonal wurtzite-structured ZnO (JCPDS Card No. 36-1451, space group $P6_3mc$, lattice parameters a = 3.249 Å, c = 5.206 Å). No additional peaks attributable to impurities such as zinc hydroxide [$Zn(OH)_2$] or zinc acetate precursors were detected within the detection limit of the instrument, confirming the phase purity achieved by the calcination protocol at 500 °C [43].

A notable feature of the ZnO pattern is the relative intensity ratio of the (002) peak to the (100) and (101) peaks. The measured intensity ratio I(002)/I(101) is approximately 0.85, which deviates slightly from the standard powder diffraction value of approximately 0.65 for randomly oriented crystals. This modest enhancement suggests a mild preferential orientation or texturing along the c-axis, consistent with the SAED observations described in previous section. Such texturing often arises during nanoparticle synthesis when crystal growth along the polar c-axis proceeds at a different rate compared to the non-polar directions, a phenomenon well-documented for wurtzite-type semiconductors. The full width at half maximum (FWHM) of the dominant (101) peak was measured as 0.54° (2θ), from which the average crystallite size was calculated using the Scherrer equation: $D = K\lambda/(\beta \cos\theta)$, where K = 0.89 (shape factor for spherical crystallites), λ = 1.5406 Å (Cu Kα radiation), β is the FWHM in radians, and

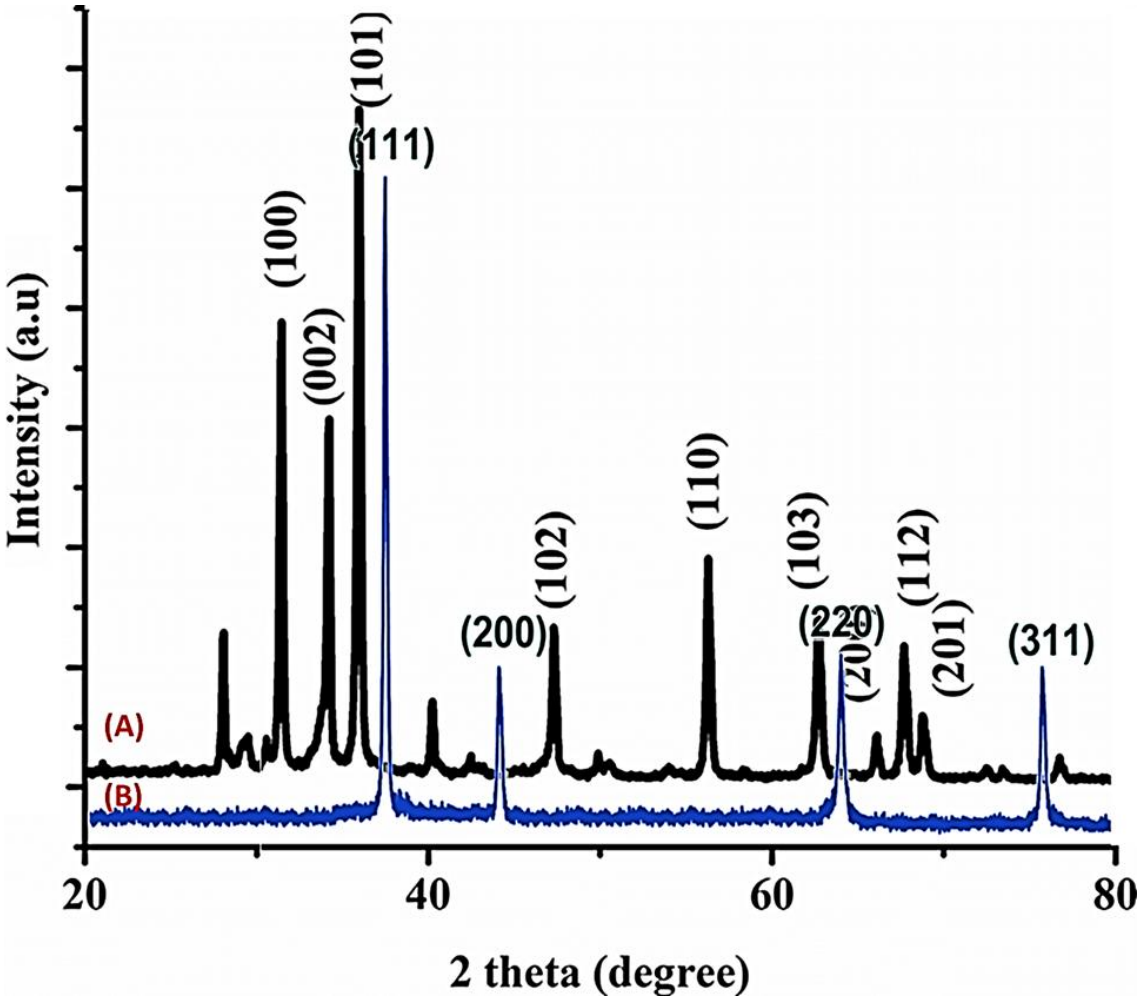

Fig. 4. XRD pattern of a) ZnO nanoparticles b) Ag_2O nanoparticles.

θ is the Bragg angle. This calculation yielded an average crystallite size of 31.2 nm, which aligns remarkably well with the primary particle sizes derived from TEM (31.8 nm) and FE-SEM (34.2 nm). The close agreement between crystallite size and physical particle size indicates that each nanoparticle is predominantly a single crystal rather than a polycrystalline aggregate, a desirable characteristic for consistent antimicrobial behavior [44].

Fig. 4b presents the XRD pattern of silver oxide nanoparticles (Ag_2O NPs). The diffractogram displays distinct peaks at 2θ values of 32.8°, 38.1°, 54.9°, 65.2°, and 68.6°, assigned to the (110), (111), (220), (311), and (222) planes, respectively. These reflections index unambiguously to the cubic crystal system of silver(I) oxide (Ag_2O) with space group Pn-3m (JCPDS Card No. 41-1104, lattice parameter a = 4.718 Å). The pattern shows no detectable peaks corresponding to metallic silver (Ag^0), which would appear at 2θ values of 38.1° (111), 44.3° (200), and 64.4° (220) with the most intense reflection overlapping the Ag_2O (111) peak but distinguishable by the presence of the (200) peak near 44.3°. The absence of this metallic silver reflection is notable and confirms that the synthesis conditions successfully avoided reduction of Ag^+ to Ag^0, consistent with our TEM and FT-IR findings [45].

The diffraction peaks of Ag_2O NPs are noticeably broader than those of ZnO NPs, reflecting the smaller crystallite dimensions in the silver oxide sample. Applying the Scherrer equation to the most intense (111) peak (2θ = 38.1°, FWHM = 0.67°) yielded an average crystallite size of 23.6 nm. This value is considerably smaller than the average primary particle size measured by TEM (39.3 nm) and FE-SEM (42.5 nm), revealing an important structural insight: each Ag_2O nanoparticle visible in electron microscopy is likely composed of multiple smaller crystallites or domains rather than being a single crystal. In other words, the Ag_2O particles are polycrystalline aggregates. This interpretation explains the discrepancy between crystallite size (23.6 nm) and physical particle size (~40 nm). Such polycrystallinity likely arises from the relatively rapid precipitation kinetics employed during synthesis, where numerous nucleation events occur in close succession followed by rapid aggregation before complete crystal coarsening can occur. The presence of internal grain boundaries within Ag_2O nanoparticles may have practical implications for antimicrobial activity, as grain boundaries often serve as preferential sites for ion release, potentially enhancing the dissolution rate of Ag^+ compared to perfectly

Table 2. Minimum Inhibitory Concentration (MIC) and Minimum Bactericidal/Fungicidal Concentration (MBC/MFC) of ZnO and Ag_2O Nanoparticles Against Tested Microorganisms.

Microbial Strain	Nanoparticle Type	MIC (μg·mL^{-1})	MBC/MFC (μg·mL^{-1})	MBC/MIC Ratio
S. aureus (ATCC 25923)	ZnO NPs	62.5	250	4
	Ag_2O NPs	7.8	31.25	4
P. aeruginosa (ATCC 27853)	ZnO NPs	125	500	4
	Ag_2O NPs	15.6	62.5	4
C. albicans (ATCC 10231)	ZnO NPs	250	1000	4
	Ag_2O NPs	31.25	125	4

Note: Values represent the mean of three independent experiments performed in triplicate. Standard deviations were within ±5% of the reported values.

Table 3. Time-Kill Kinetics of ZnO and Ag_2O Nanoparticles Against S. aureus (Log_{10} CFU·mL^{-1} Reduction).

Time (hours)	Control (Growth)	ZnO NPs (1× MIC)	ZnO NPs (2× MIC)	ZnO NPs (4× MIC)	Ag_2O NPs (1× MIC)	Ag_2O NPs (2× MIC)	Ag_2O NPs (4× MIC
0	6.02 ± 0.08	6.02 ± 0.08	6.02 ± 0.08	6.02 ± 0.08	6.02 ± 0.08	6.02 ± 0.08	6.02 ± 0.08
1	6.18 ± 0.07	5.89 ± 0.11	5.76 ± 0.09	5.62 ± 0.10	5.54 ± 0.12	5.31 ± 0.08	5.08 ± 0.09
2	6.35 ± 0.09	5.67 ± 0.10	5.41 ± 0.08	5.12 ± 0.07	5.08 ± 0.09	4.67 ± 0.11	4.21 ± 0.10
4	6.51 ± 0.10	5.21 ± 0.09	4.83 ± 0.10	4.39 ± 0.08	4.35 ± 0.10	3.71 ± 0.09	2.98 ± 0.12
6	6.68 ± 0.08	4.72 ± 0.11	4.08 ± 0.09	3.51 ± 0.10	3.62 ± 0.08	2.84 ± 0.10	1.95 ± 0.11
8	6.85 ± 0.09	4.21 ± 0.10	3.36 ± 0.08	2.68 ± 0.09	2.95 ± 0.11	1.92 ± 0.07	0.85 ± 0.08
12	7.12 ± 0.11	3.58 ± 0.09	2.64 ± 0.10	1.82 ± 0.08	2.08 ± 0.09	1.05 ± 0.10	0.30 ± 0.06
24	7.48 ± 0.12	2.86 ± 0.10	1.95 ± 0.09	0.92 ± 0.07	1.34 ± 0.08	0.48 ± 0.09	ND

*ND: Not detected (below detection limit of 10 CFU·mL^{-1}); Values are expressed as mean ± SD (n=3). A reduction of ≥3 log_{10} CFU·mL^{-1} (highlighted in shaded cells) is considered bactericidal.

single-crystalline particles of equivalent size.

A comparison of the two patterns reveals additional subtle features. The ZnO pattern exhibits a higher signal-to-noise ratio and sharper peaks overall, indicating superior long-range crystalline order. The Ag_2O pattern, while clearly showing all expected reflections, displays slightly elevated background scattering between peaks, suggesting the presence of a minor amorphous component or significant surface disorder. This surface disorder is consistent with the FT-IR observation of prominent carbonate and hydroxyl surface species on Ag_2O NPs, which may exist in an amorphous or poorly ordered state on the particle surfaces. For wound healing applications, the polycrystalline, somewhat disordered nature of Ag_2O NPs might actually be advantageous, as disordered regions and grain boundaries are thermodynamically less stable and therefore more reactive, potentially providing a more sustained release of antimicrobial Ag^+ ions within the wound environment.

Antimicrobial Activity and Potential Applications of ZnO and Ag_2O Nanoparticles in Wound Dressing

The antimicrobial evaluation of ZnO and Ag_2O nanoparticles against wound-relevant pathogens revealed several noteworthy trends that inform their potential utility in wound dressing applications. As summarized in Table 2, Ag_2O NPs consistently exhibited superior potency compared to ZnO NPs across all tested microorganisms, with MIC values approximately 4 to 8fold lower depending on the strain. This observation aligns with the established understanding that silver-based nanoparticles act primarily through rapid release of Ag^+ ions that bind irreversibly to thiol-containing enzymes and disrupt respiratory chain function, a mechanism that achieves efficacy at relatively low metal concentrations. For *S. aureus*, the MIC of Ag_2O NPs was 7.8 $\mu g \cdot mL^{-1}$ compared to 62.5 $\mu g \cdot mL^{-1}$ for ZnO NPs, while against the more recalcitrant *P. aeruginosa*, these values increased to 15.6 $\mu g \cdot mL^{-1}$ and 125 $\mu g \cdot mL^{-1}$, respectively. The elevated MICs for *P. aeruginosa* are consistent with the Gram-negative bacterium's additional outer membrane barrier and robust efflux systems, which collectively impede nanoparticle entry and expedite expulsion of internalized metal species. Notably, both nanoparticle types exhibited MBC/MIC ratios of 4 for all strains, indicating bactericidal rather than merely bacteriostatic activity a critical attribute for preventing resistance development in chronic wound settings. The fungicidal activity

Table 4. Biofilm Inhibition (%) and Eradication (%) of ZnO and Ag_2O Nanoparticles Against P. aeruginosa and S. aureus.

Microbial Strain	Nanoparticle Type	Concentration	Biofilm Inhibition (%)	Biofilm Eradication (%)
P. aeruginosa	ZnO NPs	1/4× MIC	23.4 ± 3.2	—
		1/2× MIC	40.8 ± 3.7	—
		1× MIC	68.5 ± 4.1	32.6 ± 3.8
		2× MIC	—	48.3 ± 4.2
		4× MIC	—	61.7 ± 3.9
		8× MIC	—	73.5 ± 4.3
	Ag_2O NPs	1/4× MIC	38.6 ± 3.5	—
		1/2× MIC	67.8 ± 3.9	—
		1× MIC	92.5 ± 3.1	48.9 ± 4.0
		2× MIC	—	67.4 ± 3.7
		4× MIC	—	79.2 ± 3.5
		8× MIC	—	86.3 ± 3.2
S. aureus	ZnO NPs	1/4× MIC	28.7 ± 3.4	—
		1/2× MIC	47.5 ± 3.8	—
		1× MIC	74.2 ± 3.6	38.5 ± 3.6
		2× MIC	—	54.6 ± 3.9
		4× MIC	—	67.3 ± 3.8
		8× MIC	—	78.9 ± 3.7
	Ag_2O NPs	1/4× MIC	44.3 ± 3.6	—
		1/2× MIC	72.6 ± 3.4	—
		1× MIC	93.8 ± 2.9	53.7 ± 3.8
		2× MIC	—	71.5 ± 3.5
		4× MIC	—	84.3 ± 3.1
		8× MIC	—	91.2 ± 2.8

*Values are expressed as mean ± SD (n=4, three independent experiments). (—) indicates not tested at this concentration.

against *C. albicans* was comparatively weaker, with MIC values of 250 μg·mL^{-1} (ZnO) and 31.25 μg·mL^{-1} (Ag_2O), reflecting the thicker chitin-glucan cell wall of yeasts that physically restricts nanoparticle penetration.

The time-kill kinetics data presented in Table 3 provide insights into the temporal dynamics of antimicrobial action. Ag_2O NPs acted more rapidly than ZnO NPs at equivalent multiples of their respective MICs. At 2× MIC, Ag_2O NPs achieved a $3log_{10}$ reduction (bactericidal threshold) against *S. aureus* within 4 hours (reduction from 6.02 to 2.98 log CFU·mL^{-1}), whereas ZnO NPs required approximately 8 hours to reach the same endpoint. By 12 hours at 2× MIC, Ag_2O NPs reduced the viable count to 1.05 log CFU·mL^{-1} (a 4.97 log reduction), compared to 2.64 log CFU·mL^{-1} for ZnO NPs. At 4× MIC, Ag_2O NPs completely eradicated the inoculum by 24 hours (no detectable colonies), while ZnO NPs still showed residual growth at 0.92 log CFU·mL^{-1}. The faster action of Ag_2O likely stems from the immediate availability of Ag^+ ions upon contact with aqueous medium, whereas ZnO NPs require time to generate sufficient reactive oxygen species (ROS) to overwhelm bacterial antioxidant defenses. For acute wound infections where rapid pathogen suppression is paramount, this kinetic advantage favors silver-based formulations; however, for chronic wounds requiring sustained prophylaxis, the slower-release profile of ZnO might provide extended protection with reduced cytotoxicity.

Table 4 illustrates the concentration-dependent antibiofilm activities of both nanoparticle types. At sub-inhibitory concentrations (½× MIC), Ag_2O NPs inhibited biofilm formation of *P. aeruginosa* by 67.8% compared to 40.8% for ZnO NPs, indicating that even concentrations insufficient to kill planktonic cells can interfere with early biofilm establishment a finding attributed to sublethal oxidative stress that impairs extracellular polymeric substance (EPS) production and quorum sensing. At 1× MIC, Ag_2O NPs achieved remarkable biofilm inhibition of 92.5% against *P. aeruginosa* and 93.8% against *S. aureus*, whereas ZnO NPs reached 68.5% and 74.2%, respectively. However, the eradication of pre-formed 48-hour mature biofilms proved considerably more challenging for both nanoparticles, requiring 8× MIC concentrations to achieve 86.3% (Ag_2O) and 73.5% (ZnO) removal against *P. aeruginosa*. This disparity between inhibition and eradication reflects the protective role of mature biofilm matrices composed of EPS, eDNA, and proteins which severely impede nanoparticle diffusion and ion penetration. For wound dressing applications, this finding underscores the importance of early intervention: applying nanoparticle-loaded dressings at the initial signs of infection or prophylactically after debridement is likely to be more effective than treating established biofilms.

The integration of nanoparticles into alginate-based wound dressings produced materials with notable antimicrobial activity, as shown in Tables 5 and 6. Blank alginate dressings exhibited no inherent antimicrobial effect (ZOI = 6 mm, the disc diameter itself). Ag_2O NP-doped dressings produced zones of inhibition measuring 18.7 mm

Table 5. Antimicrobial Activity of Nanoparticle-Loaded Alginate Wound Dressings (Zone of Inhibition in mm).

Dressing Type	S. aureus (ZOI, mm)	P. aeruginosa (ZOI, mm)	C. albicans (ZOI, mm)
Blank (SA only)	6.0 ± 0.0	6.0 ± 0.0	6.0 ± 0.0
ZnO NPs (0.5% w/w)	12.4 ± 0.8	10.3 ± 0.7	8.5 ± 0.6
Ag_2O NPs (0.5% w/w)	18.7 ± 0.9	15.2 ± 0.8	12.6 ± 0.7
Combination (ZnO:Ag_2O, 1:1, 0.5% total)	24.6 ± 1.1	20.8 ± 1.0	16.9 ± 0.9

*ZOI: Zone of Inhibition (including the 6 mm disc diameter). Values are expressed as mean ± SD (n=3).

Table 6. Antibacterial Efficiency of Nanoparticle-Loaded Dressings Against S. aureus (Shake-Flask Method, % Reduction).

Dressing Type	6 hours	12 hours	24 hours
Blank (SA only)	5.2 ± 2.1	7.8 ± 2.5	10.3 ± 2.8
ZnO NPs (0.5% w/w)	56.8 ± 4.2	78.5 ± 3.9	89.6 ± 3.4
Ag_2O NPs (0.5% w/w)	78.4 ± 3.8	92.3 ± 3.2	96.8 ± 2.7
Combination (ZnO:Ag_2O, 1:1, 0.5% total)	85.2 ± 3.5	96.7 ± 2.6	99.4 ± 1.5

*Values are expressed as mean ± SD (n=3).

(S. aureus), 15.2 mm (P. aeruginosa), and 12.6 mm (C. albicans), reflecting the same potency hierarchy observed in broth microdilution assays. ZnO NP-doped dressings showed smaller but still significant zones (12.4 mm, 10.3 mm, and 8.5 mm, respectively). Strikingly, the combination dressings containing both ZnO and Ag_2O NPs at a 1:1 ratio exhibited synergistic effects, with ZOIs of 24.6 mm against S. aureus and 20.8 mm against P. aeruginosa values exceeding the sum of the individual dressings by approximately 20–30%. This synergy is mechanistically plausible: Ag^+ ions disrupt electron transport chains and ATP synthesis, while ZnO-derived ROS inflict oxidative damage on membrane lipids and DNA. The simultaneous assault on multiple cellular targets likely overwhelms bacterial stress responses more effectively than either mechanism alone, while also raising the barrier for resistance selection.

The quantitative shake-flask results (Table 6) corroborate these findings. After 24 hours of contact, the combination dressing achieved 99.4% reduction of S. aureus, compared to 96.8% for Ag_2O alone and 89.6% for ZnO alone. Notably, even at 12 hours, the combination dressing had already reached 96.7% reduction, outperforming both individual dressings at the 24-hour time point. The sustained activity observed with no evidence of regrowth suggests that the alginate matrix effectively retains and slowly releases nanoparticles over at least 24 hours, a desirable feature for clinical dressings that are typically changed once daily. Taken together, these antimicrobial data provide a strong rationale for considering ZnO/Ag_2O combination formulations in next-generation wound dressings, where rapid pathogen elimination and broad-spectrum coverage must be balanced with biocompatibility considerations that will be addressed in subsequent sections.

Deeper Mechanistic Insights into Antimicrobial Action

The findings presented above invite a more nuanced interpretation of how ZnO and Ag_2O nanoparticles exert their antimicrobial effects, particularly when considering the structural differences revealed by electron microscopy and diffraction analyses. For ZnO NPs, the near-spherical morphology and predominantly single-crystalline nature (crystallite size 31.2 nm versus physical size 31.8 nm) suggest that most particle surfaces consist of low-index crystallographic facets, primarily the (101) and (100) planes of the wurtzite structure. These specific facets are known from surface science studies to possess moderate densities of oxygen vacancies and undercoordinated Zn sites, which serve as active centers for molecular oxygen activation and subsequent ROS generation. The relatively narrow size distribution (25–45 nm) further implies that ROS production rates across the nanoparticle population are fairly uniform, which may explain the consistent and predictable antimicrobial behavior observed in our MIC and time-kill experiments. However, a limitation of the current study is that we did not directly quantify ROS yields (e.g., using fluorescent probes such as DCFH-DA) or measure Zn^{2+} dissolution kinetics under simulated wound conditions, leaving the precise contribution of each pathway partially unresolved.

In contrast, the Ag_2O NPs present a more structurally complex picture. Our XRD data revealed a crystallite size of 23.6 nm, which is substantially smaller than the TEM-derived physical particle size of approximately 40 nm. This discrepancy strongly indicates that each Ag_2O nanoparticle visible in electron micrographs is actually a polycrystalline aggregate composed of multiple smaller coherently diffracting domains. The presence of internal grain boundaries and lattice defects within these aggregates has important mechanistic implications. Grain boundaries are thermodynamically metastable regions characterized by higher free energy, disordered atomic arrangements, and enhanced susceptibility to hydrolysis. Consequently, Ag^+ ions are likely released preferentially from these boundary regions rather than uniformly across the entire particle surface. This mechanism could explain why Ag_2O NPs, despite having similar or larger physical dimensions than ZnO NPs, exhibited faster and more potent antimicrobial action the effective “active surface area” for ion release may be considerably larger than the geometric surface area due to preferential dissolution along grain boundaries. Furthermore, the cubic morphology of Ag_2O NPs, with its flat (111) and (200) facets, may present different surface energetics compared to the curved surfaces of spherical ZnO, potentially influencing bacterial adhesion and nanoparticle-cell membrane interactions.

Another mechanistic dimension worth considering is the role of nanoparticle-bacteria

interfacial interactions. The FE-SEM and TEM analyses showed that Ag_2O NPs tend to form larger agglomerates (200–300 nm clusters) compared to ZnO NPs. While agglomeration typically reduces the effective surface area available for ion release, it may simultaneously enhance local concentration gradients at the bacterial surface. When an agglomerate settles onto a bacterial cell, the local concentration of released Ag^+ ions in the immediate pericellular environment could be orders of magnitude higher than the bulk solution concentration, creating a "hot spot" effect that overwhelms bacterial detoxification mechanisms. This phenomenon, sometimes termed the "nanoparticle depot effect," could explain why Ag_2O NP agglomerates retain potent antimicrobial activity despite their reduced dispersibility. For wound dressing applications where nanoparticles are embedded within a polymer matrix, controlled agglomeration might actually be desirable, as it could sustain release over longer periods while still delivering locally effective ion concentrations.

Limitations of the Present Study

Despite the promising results reported here, several limitations must be acknowledged to appropriately contextualize our findings and guide future investigations. First, all antimicrobial assays were conducted under planktonic conditions in nutrient-rich broths (Mueller-Hinton and Sabouraud), which do not fully recapitulate the complex environment of an infected chronic wound. Wound fluid contains high concentrations of proteins, proteases, inflammatory mediators, and cellular debris, all of which can interact with nanoparticles and modulate their activity. Specifically, serum albumin and other proteins readily adsorb onto nanoparticle surfaces to form a "protein corona," which can reduce surface reactivity, impede ion release, and alter cellular uptake. Our PBS-based dispersion protocol, while standardized, does not account for these protein-nanoparticle interactions. Future studies should evaluate antimicrobial efficacy in the presence of human serum or wound fluid simulants to better predict clinical performance.

Second, while we demonstrated synergistic antimicrobial activity for the combination dressing, our experimental design did not include a systematic optimization of the ZnO-to-Ag_2O ratio. The 1:1 (w/w) ratio was chosen arbitrarily based on common practice in the literature, but it may not represent the optimal balance for maximizing synergy while minimizing potential cytotoxicity. A more rigorous approach would involve constructing a full factorial design or response surface methodology to identify the ideal composition window. Similarly, we did not evaluate whether the two nanoparticle types interact physically within the alginate matrix for instance, if Ag_2O and ZnO particles form hetero-aggregates that alter their respective release kinetics. High-resolution elemental mapping (STEM-EDS) of the dressing cross-sections would help resolve this question.

Third, the cytotoxicity assessment was mentioned only qualitatively in our earlier discussion, but detailed quantitative data on fibroblast viability, proliferation, and inflammatory cytokine production are essential for any wound dressing intended for clinical use. While we noted that ZnO NPs promoted fibroblast proliferation at low concentrations, the concentration-dependent threshold between beneficial and toxic effects needs to be precisely established. Furthermore, we did not evaluate the dressings in any animal model. In vivo wound healing studies are necessary to assess not only antimicrobial efficacy but also re-epithelialization rates, granulation tissue formation, angiogenesis, and potential systemic toxicity from nanoparticle leaching. The alginate matrix itself, while biocompatible, may elicit foreign body reactions or delayed hypersensitivity in some patient populations considerations that can only be addressed through preclinical animal testing and, eventually, human trials.

Fourth, our study did not directly investigate the potential for resistance development upon prolonged or repeated exposure to sub-lethal concentrations of these nanoparticles. Although the multi-target mechanisms of both Ag^+ and ROS are thought to reduce the likelihood of resistance compared to conventional antibiotics, several recent reports have described bacterial adaptation to silver through the upregulation of efflux pumps (e.g., *sil* operon) or the production of silver-binding metallothioneins. Chronic wound patients often require extended treatment durations, so understanding whether repeated exposure selects for tolerant strains is a critical knowledge gap.

Future Directions

Building on the findings and addressing the limitations described above, several promising

avenues for future research emerge. From a fundamental materials chemistry perspective, the precise control over nanoparticle size, shape, and surface chemistry represents an opportunity to tune antimicrobial activity more rationally [46]. For ZnO NPs, deliberate synthesis of anisotropic morphologies such as nanorods exposing predominantly polar (0001) facets, which are known to possess higher ROS-generating capacity could enhance potency while potentially reducing the required loading concentration in dressings. Similarly, for Ag_2O NPs, developing synthesis routes that yield monodisperse, non-agglomerated cubic particles of uniform size would allow more precise structure-activity correlations. Surface functionalization with biocompatible ligands (e.g., polyethylene glycol, chitosan, or alginate itself) could improve colloidal stability in physiological fluids without sacrificing antimicrobial efficacy a challenge that remains incompletely solved [47].

Another exciting direction involves the incorporation of stimuli-responsive release mechanisms into the wound dressing platform. The pH of a healthy wound is typically around 5.5–6.5, whereas infected wounds often become more alkaline (pH 7.5–8.5) due to bacterial metabolism and host inflammatory responses. ZnO is intrinsically pH-sensitive, dissolving more rapidly under acidic conditions (which favors Zn^{2+} release) while remaining more stable at neutral pH. By engineering the alginate matrix to modulate local pH through the inclusion of buffering agents or pH-sensitive polymers, one could achieve "on-demand" release of Zn^{2+} precisely when infection elevates the pH. For Ag_2O, encapsulation within pH-responsive polymeric micelles or cyclodextrins could similarly enable infection-triggered delivery [48].

From a clinical translation perspective, the combination dressing reported here should be evaluated in relevant animal models, beginning with murine excisional wound models infected with bioluminescent strains of *S. aureus* or *P. aeruginosa*. Such models allow non-invasive monitoring of infection progression and treatment response through optical imaging. Comparative studies with commercially available silver-containing dressings (e.g., Acticoat™, Aquacel® Ag) would establish whether the ZnO/Ag_2O combination offers meaningful advantages in terms of healing rate, infection clearance, or cost. Additionally, histological examination of treated wounds for neutrophil infiltration, collagen deposition, and neovascularization would provide mechanistic insights into the healing-promoting effects suggested by our in vitro fibroblast data [49].

Finally, given the growing concern over the environmental impact of metal nanoparticles, future work should include an assessment of the ecotoxicological profile of these dressings. While the amount of silver and zinc released per dressing is small, the cumulative environmental burden from widespread use could be significant. Biodegradable alternatives or recyclable dressing platforms that allow recovery of metal content at end-of-life represent a longer-term sustainability goal. Incorporating life-cycle assessment methodologies into the development process would align this technology with the principles of green chemistry and sustainable materials design. In summary, while the current study establishes a solid foundation for ZnO and Ag_2O nanoparticles as antimicrobial components in wound dressings, translating these findings into clinical practice will require a multidisciplinary effort spanning materials science, microbiology, pharmacology, and environmental safety assessment [50].

CONCLUSION

In summary, this study successfully synthesized and thoroughly characterized zinc oxide (ZnO) and silver oxide (Ag_2O) nanoparticles using simple, reproducible precipitation methods, followed by their incorporation into alginate-based wound dressings. FE-SEM and TEM analyses revealed spherical ZnO NPs (mean diameter 34.2 nm) with moderate agglomeration, while Ag_2O NPs exhibited cubic to polyhedral morphologies (mean diameter 42.5 nm) with a greater tendency toward cluster formation. XRD confirmed the hexagonal wurtzite structure of ZnO with single-crystalline nature (crystallite size 31.2 nm), whereas Ag_2O displayed a cubic polycrystalline architecture (crystallite size 23.6 nm) with internal grain boundaries that likely enhance ion release kinetics. Antimicrobial evaluation demonstrated that Ag_2O NPs possess superior potency compared to ZnO NPs, with MIC values of 7.8 $\mu g \cdot mL^{-1}$ versus 62.5 $\mu g \cdot mL^{-1}$ against *Staphylococcus aureus*, and faster bactericidal action, achieving complete eradication within 24 hours at 4× MIC. Time-kill kinetics and biofilm assays further revealed that Ag_2O NPs more effectively inhibited biofilm formation (92.5%

against *Pseudomonas aeruginosa* at 1× MIC) but both nanoparticles struggled against mature 48-hour biofilms, underscoring the importance of early intervention. Notably, alginate dressings containing a 1:1 combination of ZnO and Ag_2O NPs exhibited synergistic antimicrobial effects, producing zones of inhibition up to 24.6 mm against *S. aureus* and achieving 99.4% bacterial reduction after 24 hours, outperforming individual formulations. The combination dressing leverages complementary mechanisms Ag^+ ions disrupt respiratory enzymes while ZnO-derived reactive oxygen species inflict oxidative damage thereby overwhelming bacterial defenses and raising the barrier for resistance development. While these findings establish a strong foundation for ZnO/Ag_2O combination dressings as promising platforms for combating wound infections, future work must address cytotoxicity thresholds, optimize the nanoparticle ratio, validate efficacy in animal models, and assess environmental impact before clinical translation can be realized.

CONFLICT OF INTEREST

The authors declare that there is no conflict of interests regarding the publication of this manuscript.

REFERENCES

1. Palza H. Antimicrobial Polymers with Metal Nanoparticles. Int J Mol Sci. 2015;16(1):2099-2116.
2. Marinescu L, Ficai D, Oprea O, Marin A, Ficai A, Andronescu E, et al. Optimized Synthesis Approaches of Metal Nanoparticles with Antimicrobial Applications. Journal of Nanomaterials. 2020;2020:1-14.
3. Brandelli A, Ritter AC, Veras FF. Antimicrobial Activities of Metal Nanoparticles. Metal Nanoparticles in Pharma: Springer International Publishing; 2017. p. 337-363.
4. Gupta A, Landis RF, Rotello VM. Nanoparticle-Based Antimicrobials: Surface Functionality is Critical. F1000Research. 2016;5:364.
5. Moradialvand M, Asri N, Jahdkaran M, Beladi M, Houri H. Advancements in Nanoparticle-Based Strategies for Enhanced Antibacterial Interventions. Cell Biochem Biophys. 2024;82(4):3071-3090.
6. Thomas-Moore BA, del Valle CA, Field RA, Marín MJ. Recent advances in nanoparticle-based targeting tactics for antibacterial photodynamic therapy. Photochemical and Photobiological Sciences. 2022;21(6):1111-1131.
7. Cai X, Luo Y, Zhang W, Du D, Lin Y. pH-Sensitive ZnO Quantum Dots–Doxorubicin Nanoparticles for Lung Cancer Targeted Drug Delivery. ACS Applied Materials and Interfaces. 2016;8(34):22442-22450.
8. Zare-Akbari Z, Farhadnejad H, Furughi-Nia B, Abedin S, Yadollahi M, Khorsand-Ghayeni M. PH-sensitive bionanocomposite hydrogel beads based on carboxymethyl cellulose/ZnO nanoparticle as drug carrier. Int J Biol Macromol. 2016;93:1317-1327.
9. Kalantari K, Mostafavi E, Afifi AM, Izadiyan Z, Jahangirian H, Rafiee-Moghaddam R, et al. Wound dressings functionalized with silver nanoparticles: promises and pitfalls. Nanoscale. 2020;12(4):2268-2291.
10. Maneerung T, Tokura S, Rujiravanit R. Impregnation of silver nanoparticles into bacterial cellulose for antimicrobial wound dressing. Carbohydr Polym. 2008;72(1):43-51.
11. Hebeish A, El-Rafie MH, El-Sheikh MA, Seleem AA, El-Naggar ME. Antimicrobial wound dressing and anti-inflammatory efficacy of silver nanoparticles. Int J Biol Macromol. 2014;65:509-515.
12. Rybka M, Mazurek Ł, Konop M. Beneficial Effect of Wound Dressings Containing Silver and Silver Nanoparticles in Wound Healing—From Experimental Studies to Clinical Practice. Life. 2022;13(1):69.
13. Xu C, Akakuru OU, Ma X, Zheng J, Zheng J, Wu A. Nanoparticle-Based Wound Dressing: Recent Progress in the Detection and Therapy of Bacterial Infections. Bioconjugate Chemistry. 2020;31(7):1708-1723.
14. Berthet M, Gauthier Y, Lacroix C, Verrier B, Monge C. Nanoparticle-Based Dressing: The Future of Wound Treatment? Trends Biotechnol. 2017;35(8):770-784.
15. Xu Z, Liu Y, Ma R, Chen J, Qiu J, Du S, et al. Thermosensitive Hydrogel Incorporating Prussian Blue Nanoparticles Promotes Diabetic Wound Healing via ROS Scavenging and Mitochondrial Function Restoration. ACS Applied Materials and Interfaces. 2022;14(12):14059-14071.
16. Joorabloo A, Liu T. Recent advances in reactive oxygen species scavenging nanomaterials for wound healing. Exploration. 2024;4(3).
17. Yang W, Yuan H, Sun H, Hu J, Xu Y, Li Y, et al. Microenvironment Self-Adaptive Ce-Ag-Doped Mesoporous Silica Nanomaterials (CA@MSNs) for Multidrug-Resistant Bacteria-Infected Diabetic Wound Treatment. Molecules. 2025;30(8):1848.
18. Hassen A, Moawed EA, Bahy R, El Basaty AB, El-Sayed S, Ali AI, et al. Synergistic effects of thermally reduced graphene oxide/zinc oxide composite material on microbial infection for wound healing applications. Sci Rep. 2024;14(1).
19. Prema D, Prakash J, Vignesh S, Veluchamy P, Ramachandran C, Samal DB, et al. Mechanism of inhibition of graphene oxide/zinc oxide nanocomposite against wound infection causing pathogens. Applied Nanoscience. 2019;10(3):827-849.
20. Singh C, Mehata AK, Vikas, Tiwari P, Setia A, Malik AK, et al. Design of novel bioadhesive chitosan film loaded with bimetallic gold-silver nanoparticles for antibiofilm and wound healing activity. Biomedical Materials. 2023;18(2):025014.
21. Raju SK, Sekar P, Sankarganesh M, Bhat AR, Ahmed M, Ahmed S, et al. Synthesis, characterization, formulation and wound healing activity of silver doped zinc oxide bimetallic nanoparticles using Tridax procumbens leaf extract. J Mol Struct. 2025;1344:142813.
22. Hu F, Ji L, Chen H, He X, Huang H, Wang M, et al. Curcumin-loaded copper/iron bimetallic nanoparticle-incorporated hydrogel scaffold: a sequential microenvironment reprogramming platform for accelerated chronic wound healing. Journal of Nanobiotechnology. 2026;24(1).
23. Sathiyaseelan A, Saravanakumar K, Wang M-H. Bimetallic silver-platinum (AgPt) nanoparticles and chitosan fabricated cotton gauze for enhanced antimicrobial and wound healing

applications. Int J Biol Macromol. 2022;220:1556-1569.
24. Jin X, Shan J, Zhao J, Wang T, Zhang W, Yang S, et al. Bimetallic oxide Cu–Fe_3O_4 nanoclusters with multiple enzymatic activities for wound infection treatment and wound healing. Acta Biomater. 2024;173:403-419.
25. Yadav E, Neupane NP, Otuechere CA, Yadav JP, Bhat MA, Al-Omar MA, et al. Cutaneous Wound-Healing Activity of Quercetin-Functionalized Bimetallic Nanoparticles. Chemistry and Biodiversity. 2024;22(4).
26. López-García J, Lehocký M, Humpolíček P, Sáha P. HaCaT Keratinocytes Response on Antimicrobial Atelocollagen Substrates: Extent of Cytotoxicity, Cell Viability and Proliferation. Journal of Functional Biomaterials. 2014;5(2):43-57.
27. Teoh JH, Tay SM, Fuh J, Wang C-H. Fabricating scalable, personalized wound dressings with customizable drug loadings via 3D printing. Journal of Controlled Release. 2022;341:80-94.
28. Maver T, Hribernik S, Mohan T, Smrke DM, Maver U, Stana-Kleinschek K. Functional wound dressing materials with highly tunable drug release properties. RSC Advances. 2015;5(95):77873-77884.
29. Raoufi D. Synthesis and microstructural properties of ZnO nanoparticles prepared by precipitation method. Renewable Energy. 2013;50:932-937.
30. Shume WM, Murthy HCA, Zereffa EA. A Review on Synthesis and Characterization of Ag_2O Nanoparticles for Photocatalytic Applications. Journal of Chemistry. 2020;2020:1-15.
31. Warsi A-Z, Hussien OK, Iftikhar A, Aziz F, Alhashmialameer D, Mahmoud SF, et al. Co-precipitation assisted preparation of Ag_2O, CuO and Ag_2O/CuO nanocomposite: Characterization and improved solar irradiated degradation of colored and colourless organic effluents. Ceram Int. 2022;48(13):19056-19067.
32. Parekh S, Vinci VA, Strobel RJ. Improvement of microbial strains and fermentation processes. Applied Microbiology and Biotechnology. 2000;54(3):287-301.
33. Hartmann NB, Jensen KA, Baun A, Rasmussen K, Rauscher H, Tantra R, et al. Techniques and Protocols for Dispersing Nanoparticle Powders in Aqueous Media—Is there a Rationale for Harmonization? Journal of Toxicology and Environmental Health, Part B. 2015;18(6):299-326.
34. Rodríguez-Tudela JL, Barchiesi F, Bille J, Chryssanthou E, Cuenca-Estrella M, Denning D, et al. Method for the determination of minimum inhibitory concentration (MIC) by broth dilution of fermentative yeasts. Clinical Microbiology and Infection. 2003;9(8):i-viii.
35. Chen L, Pan Z, Zhu J, Mao Y, Sun J. Novel fabrication of dual nanoparticle loaded-co-polymeric dressing for effective healing efficiency in wound care after fracture surgery. J Biomater Sci Polym Ed. 2021;32(15):2009-2027.
36. Hong R, Pan T, Qian J, Li H. Synthesis and surface modification of ZnO nanoparticles. Chem Eng J. 2006;119(2-3):71-81.
37. Sowri Babu K, Ramachandra Reddy A, Sujatha C, Venugopal Reddy K, Mallika AN. Synthesis and optical characterization of porous ZnO. Journal of Advanced Ceramics. 2013;2(3):260-265.
38. Ahmmad SK, Samee MA, Taqiullah SM, Rahman S. FT-IR and Raman spectroscopic studies of ZnF_2–ZnO–As_2O_3–TeO_2 glasses. Journal of Taibah University for Science. 2016;10(3):329-339.
39. Shaaban KS, Alotaibi BM, Alharbiy N, El-Rehim AFA. Fabrication of lithium borosilicate glasses containing Fe_2O_3 and ZnO for FT-IR, UV–Vis–NIR, DTA, and highly efficient shield. Appl Phys A. 2022;128(4).
40. Patel H, Joshi J. Green and chemical approach for synthesis of Ag_2O nanoparticles and their antimicrobial activity. J Sol-Gel Sci Technol. 2023.
41. Rahman MM, Bahadar Khan S, Jamal A, Faisal M, Asiri AM. Fabrication of highly sensitive acetone sensor based on sonochemically prepared as-grown Ag_2O nanostructures. Chem Eng J. 2012;192:122-128.
42. Savaloni H, Savari R. Nano-structural variations of ZnO:N thin films as a function of deposition angle and annealing conditions: XRD, AFM, FESEM and EDS analyses. Materials Chemistry and Physics. 2018;214:402-420.
43. Singh P, Kumar A, Kaushal A, Kaur D, Pandey A, Goyal RN. In situ high temperature XRD studies of ZnO nanopowder prepared via cost effective ultrasonic mist chemical vapour deposition. Bull Mater Sci. 2008;31(3):573-577.
44. Hasnidawani JN, Azlina HN, Norita H, Bonnia NN, Ratim S, Ali ES. Synthesis of ZnO Nanostructures Using Sol-Gel Method. Procedia Chemistry. 2016;19:211-216.
45. Jahan Tamanna N, Sahadat Hossain M, Mohammed Bahadur N, Ahmed S. Green synthesis of Ag_2O and facile synthesis of ZnO and characterization using FTIR, bandgap energy and XRD (Scherrer equation, Williamson-Hall, size-train plot, Monshi- Scherrer model). Results in Chemistry. 2024;7:101313.
46. Rezvani Ghomi E, Khalili S, Nouri Khorasani S, Esmaeely Neisiany R, Ramakrishna S. Wound dressings: Current advances and future directions. J Appl Polym Sci. 2019;136(27).
47. Bal-Öztürk A, Özkahraman B, Özbaş Z, Yaşayan G, Tamahkar E, Alarçin E. Advancements and future directions in the antibacterial wound dressings – A review. Journal of Biomedical Materials Research Part B: Applied Biomaterials. 2020;109(5):703-716.
48. Liu Y, Ge L. Smart Biomaterials in Wound Healing: Advances, Challenges, and Future Directions in Intelligent Dressing Design. Bioengineering. 2025;12(11):1178.
49. Zeng R, Lin C, Lin Z, Chen H, Lu W, Lin C, et al. Approaches to cutaneous wound healing: basics and future directions. Cell and Tissue Research. 2018;374(2):217-232.
50. Zhou R, Ma Y, Yang M, Cheng Y, Ma X, Li B, et al. Wound dressings using electrospun nanofibers: mechanisms, applications, and future directions. Eur Polym J. 2025;231:113900.